Techno-economic optimisation of a sodium{ extendash}chloride salt heat exchanger for concentrating solar power applications

Solar Energy 239 (2022) 252–267

Contents lists available at ScienceDirect

Solar Energy

journal homepage: www.elsevier.com/locate/solener

Techno-economic optimisation of a sodium–chloride salt heat exchanger for concentrating solar power applications

Salvatore Guccione [a,*], Armando Fontalvo [b], Rafael Guedez [a], John Pye [b], Laura Savoldi [c], Roberto Zanino [c]

[a] Department of Energy Technology, KTH Royal Institute of Technology, Stockholm, 10044, Sweden
[b] School of Engineering, The Australian National University, Canberra, 2600, ACT, Australia
[c] Dipartimento Energia "Galileo Ferraris", Politecnico di Torino, Turin, 10129, Italy

ARTICLE INFO

Keywords:
CSP
Sodium
Chloride salt
Heat exchanger
Techno-economic optimisation

ABSTRACT

To enhance the economic viability of Concentrating solar power (CSP) plant, recent efforts have been directed towards employing high-temperature working fluid in the receiver and incorporating higher-efficiency power cycles. This work presents a techno-economic analysis of a sodium–chloride salt heat exchanger included in a sodium-driven CSP system with a supercritical CO_2 power block. A quasi-steady state heat exchanger model was developed based on the TEMA guidelines, with the possibility of being customised in terms of media adopted, constraints, boundary conditions, and heat transfer correlations. The sodium–salt heat exchanger has been designed aiming at minimising the Levelized Cost of Electricity (LCOE) of the plant. The performance and the design of the proposed heat exchanger have been evaluated via multi-objective optimisation and sensitivity analyses. Results show that advanced CSP systems employing sodium and an indirect chloride salt storage can represent an economically viable solution and can drive towards the future goal of 5 USD/MWh. For a base-case 100 MW_e plant with 12 h of storage, a LCOE of 72.7 USD/MWh and a capacity factor (CF) higher than 60% were reached. The techno-economic investigations showed the potential LCOE reduction of 6% as well as the flexibility and robustness of the heat exchanger model. The developed tool lays the groundwork to explore potential improvements of this new generation of CSP systems.

1. Introduction

Concentrating solar power (CSP) is one of the most promising renewable energy-based electricity generation technologies to deal with the increasing demand for power consumption and environmental sustainability (Fritsch et al., 2019). The added value of this technology is the integration of a thermal energy storage (TES) that increases the system stability, dispatchability, and the duration of energy output. The USA Solar Energy Technologies Office (SETO) aims to achieve by 2030 an electricity cost of 5 USD/MWh for base-load configurations of CSP with 12 or more hours of thermal energy storage (Murphy et al., 2019). To increase the economic competitiveness of CSP plants, the adoption of advanced high-temperature working fluids and the integration sCO_2 power blocks are considered to be essential next steps (DOE, 2012).

As a possible alternative to conventional molten salt, high-temperature particles can be employed both as receiver heat transfer fluid and as storage media (Ho, 2016; Gunawan Gan et al., 2021). Another alternative is represented by gas-based receivers coupled to suitable energy storage systems, for example, packed bed (Trevisan et al., 2020), thermocline, and phase change material systems. Sodium is also identified as a promising heat transfer fluid that can be employed in CSP applications to increase the plant overall efficiency and reduce the investment cost (Fritsch et al., 2019; Wood and Drewes, 2019). The big advantages of liquid sodium are the higher maximum acceptable temperatures (98 °C to 890 °C) and the high heat conductivity that leads to very high heat transfer coefficients compared to conventional molten salts (Zheng et al., 2020). Consequently, employing sodium as heat transfer fluid (HTF), more compact, cheaper and more thermally efficient receivers can be designed (Coventry et al., 2015). On the contrary, the main disadvantage of sodium concerns its reactivity with water and oxygen, which could result in fires. Due to cost, sodium is not suitable as a bulk thermal energy storage medium (Blanco and Santigosa, 2017), leading to the investigation of storage concepts, including two-tank sensible systems, phase change material (Kee et al., 2020; de la Calle et al., 2020), and packed bed/thermocline storage (Niedermeier et al., 2018). A two-tank storage system employing advanced high-temperature molten chloride salt has been identified as

* Correspondence to: Department of Energy Technology, KTH Royal Institute of Technology, Brinellvägen 68, Stockholm, Sweden.
E-mail address: guccione@kth.se (S. Guccione).

https://doi.org/10.1016/j.solener.2022.04.052
Received 5 December 2021; Received in revised form 2 March 2022; Accepted 21 April 2022
Available online 17 May 2022

Nomenclature

Abbreviations

ASME	American Society of Mechanical Engineers
ASTRI	Australian Solar Thermal Research Institute
BOP	balance of plant
CO_2	carbon dioxide
CAPEX	capital expenditure
CEPCI	Chemical Plant Cost Index
CF	capacity factor
CRF	capital recovery factor
CS	chloride salt
CSP	concentrating solar power
DNI	direct normal irradiance
EPY	energy per year
H230	Haynes230
HTC	heat transfer coefficient
HTF	heat transfer fluid
HX	heat exchanger
KPI	key performance indicator
LCOE	levelized cost of electricity
LMTD	log-mean temperature difference
OPEX	operating expenditure
PSA	Plataforma Solar de Almería
sCO_2	supercritical carbon dioxide
SM	solar multiple
STHE	shell and tube heat exchanger
TAC	total annualised cost
TEMA	Tubular Exchanger Manufacturers Association
TES	thermal energy storage
TIT	turbine inlet temperature
USD	United States Dollar

Greek Symbols

α	absorption coefficient [–]
Δp	pressure drop [Pa]
η	efficiency [–]
λ	thermal conductivity [W/(m K)]
μ	dynamic viscosity [Pa s]
ρ	density [kg/m^3]
θ	angle [rad]

Symbols

$\dot{m}$	mass flow rate [kg/s]
A	area [m^2]
C	cost [USD]
c	specific cost
D	diameter [m]
d	tube diameter [m]
f'	real discount rate [–]
F	factor [–]
f	nominal discount rate [–]
H	height [m]
h	specific enthalpy [J/kg]
h_s	shell-side heat transfer coefficient [W/(m^2 K)]
h_t	tube-side heat transfer coefficient [W/(m^2 K)]
i	inflation rate [–]
J	correction factor for the shell-side HTC [–]
j_f	dimensionless friction factor [–]
L	length [m]
l	spacing [m]
M_a	mass over area factor [kg/m^2]
N	number [–]
Nu	Nusselt non-dimensional number [–]
P	pitch [m]
p	pressure [Pa]
Pe	Peclet non-dimensional number [–]
Q	thermal power [W]
R_s	fouling resistance [(m^2 K)/W]
Re	Reynolds non-dimensional number [–]
S	shell internal area [m^2]
T	temperature [K]
t	thickness [m]
tm	operating time [hours]
U	total heat transfer coefficient [W/(m^{2}K)]
UA	overall heat transfer coefficient [W/K]
v	fluid velocity [m/s]

Subscripts

B	bundle bypass
b	baffle
bb	bundle-to-shell clearance
bp	bypass
bu	tube bundle
C	baffle cut and spacing
c	cross-flow
cf	cross-flow free length
cs	cross section
ctl	centriangle
cw	effective tubes in the window
des	design
e	entrance and exit region
i	internal
id	ideal
in	inlet
inv	investment
L	baffle clearance
M	material
ma	manufacturing
ml	mean-log
o	outside
out	outlet
P	pressure
p	passes
par	parasitic
req	required
s	shell
sb	shell-to-baffle
sp	shell passes
ss	sealing strips
t	tube
tb	tube-to-baffle
tw	tubes in the window
w	window region
wg	gross window region
y	years

the most promising configuration for sodium-based CSP plants (DOE, 2018). The ternary chloride salt eutectic mixtures of NaCl-KCl-$MgCl_2$ stands out for the operating temperatures higher than 700 °C and their costs significantly lower than conventional solar salts (Ho and Iverson, 2014; Mohan et al., 2018). Nevertheless, low-maturity, material compatibility, and corrosion are fundamental issues that need to be addressed.

In this context, the sodium-salt HX represents a crucial component for the integration and feasibility of this type of next-generation CSP plants. Even though heat exchangers account for a small percentage in terms of capital expenditure (CAPEX) of the CSP plants, their failure due to excessive thermo-mechanical loading could hinder the performance of the power plant both from a technical and economic perspective (Ferruza, 2018; Price et al., 2021). Issues related to the design of CSP heat exchangers have generally been reported by plant operators to be associated with the tube and tube–sheet connections due to the cyclic nature and high-temperature gradients experienced during the operation of these plants (Price et al., 2021). Despite the crucial role of the intermediate or primary heat exchangers for the feasibility, availability, and reliability of the CSP plants, the importance of a detailed design of such components has often been underestimated during techno-economic analysis in the field. A comprehensive model for multi-pass shell and tube heat exchanger (STHE) has been introduced, focusing on transient responses for constant design parameters, with no cost-analysis involved (Bonilla et al., 2017). Techno-economic analyses for the design of heat exchangers in CSP were conducted tailoring the model for steam generators (Ferruzza et al., 2019). In a sodium-based CSP system with conventional Solar Salt TES, the sodium-to-salt HX was modelled with fixed effectiveness and a fixed specific cost (Fritsch et al., 2019). In similar studies, where Solar Salt was employed as HTF in the receiver and storage media in the TES the primary heat exchanger was model with constant effectiveness and its cost was included in the Balance of Plant (BOP) (Zurita et al., 2018). Similarly, for particle-based systems, a fixed effectiveness approach and a cost function of the overall heat transfer coefficient (UA) was adopted (González-portillo et al., 2021).

The absence of a sodium–chloride salt heat exchanger design and the lack of comprehensive techno-economic studies of sodium-based CSP systems with chloride salt TES are the motivation for this work. The lack of a flexible, customisable, easily integrated, and open-source heat exchanger model for supporting techno-economic studies of novel CSP plants has been identified. In order to fill the identified literature gaps, this study proposes a techno-economic analysis of a sodium–chloride salt heat exchanger included in a sodium-based CSP system with a sCO_2 power block. Fig. 1 shows a schematic representation of the investigated CSP layout. A novel sodium-to-chloride salt heat exchanger design has been defined by developing a reusable and general model for STHE and integrating it into a newly-developed sodium–salt–sCO_2 CSP system model. The heat exchanger model proposes a design, with costs and performance estimation resulting from an optimisation of the internal geometry configuration for an ad-hoc defined objective function. Moreover, the developed model offers the possibility of being customised in terms of media adopted, constraints, boundary conditions, and heat transfer correlations. When integrated in the CSP plant, the design of the heat exchanger has been optimised to minimise the LCOE of the plant.

The paper first presents the heat exchanger model in Section 2. An integrated system model of a novel CSP plant – combining a tubular sodium receiver, the sodium-to-chloride salt STHE, two-tank chloride salt TES and sCO_2 power block – is next presented (Section 3). The method of optimising the sodium-to-chloride salt heat exchanger design and its operating temperatures is described in Section 4. Results include the HX internal configuration, overall HX temperature difference, and an analysis of cost sensitivities (Section 5). A discussion (Section 6) is followed by Conclusions (Section 7).

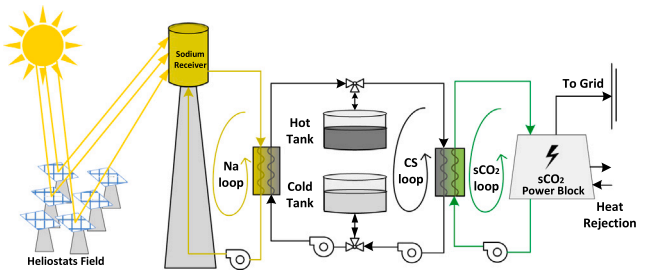

Fig. 1. Sodium driven CSP plant with two tank chloride salt TES and integrated with a sCO_2 power block.

1.1. Sodium safety concerns

Addressing sodium safety concerns is fundamental for pervasive acceptance of CSP at megawatt or gigawatt scales. Fire and operational instabilities are the dominant contributors to risk events for advanced sodium high-temperature solar power systems. Sodium has mainly been employed as a high-temperature working fluid within the nuclear power industry (Jordan et al., 1988; Simons and Basham, 1966), providing significant practical experience about liquid sodium safety. Two of the most common safety risks associated with sodium are its reactions with water and with air that result in violent explosions. Thus, keeping sodium completely isolated is a fundamental safety rule. A sodium fire is extinguished by the removal of oxygen, or by suppressing oxygen with inert gas or by preventing oxygen replenishment as the fire burns (Coventry et al., 2015).

The most well-known sodium fire in the CSP community was the sodium spray fire accident at the Plataforma Solar de Almería (PSA) facility in 1986, during maintenance works on the plant with the storage tanks pressurised (MCCE, 1987). A less major incident in the CSP field was a sodium fire at the Vast Solar pilot plant during pre-commissioning tests in 2015, caused by a leak from a flanged pipe connection that connected field piping to a sodium storage tank (Vast Solar, 2015). These incidents reinforce that sodium is a hazardous substance and that in developing CSP installations with sodium, high standards of safety design and operator training are necessary. CSP receiver can be realised through the implementation of handling and engineering controls (Bucher, 1983), guaranteeing safe and optimal heat transfer performance. Complexity in process equipment has been linked to accident risk in hazardous environments (Wolf, 2001), and it is noted that a sodium HTF loop in a CSP plant is considerably simpler than what is seen in other well-accepted industrial plants involving hazardous materials, such as petrochemical refineries.

2. Heat exchanger model

The heat exchanger model was developed as a versatile and general model, tailored for shell and tubes heat exchangers. It can be employed for several applications and used with different media. The model was implemented using the object-oriented Modelica programming language. The model was developed using Python 3.8.8 and Matlab R2020b to extend its applicability.[1] The general assumptions included in the model are

- adoption of a lumped-parameter model,
- adoption of a quasi-static model,
- negligible thermal losses,
- adoption of the log-mean temperature difference (LMTD) approach, and

[1] The heat exchanger model can be found at: https://github.com/S-Guccione/SodiumChlorideSaltHX.git.

- adoption of Tubular Exchanger Manufacturers Association (TEMA) standards.

Two possible shell and tube configurations are built-in in this model: one shell pass, one tube pass (1 : 1 TEMA E STHE), and two shell passes, two tube passes (2 : 2 TEMA F STHE). Fig. 2 shows the aforementioned layouts, which include tilted baffles to facilitate drainage, and heated baffles to avoid freezing as two design variations compared to the standard TEMA configurations.

As it is safer to allocate the cold fluid around the hot fluid, as well as, it reduces energy losses and the overall equipment cost (Incropera and Dewitt, 1981), the hot fluid is placed on the tube-side, while the cold fluid is on the shell-side. The model proposes a suitable design of a shell and tube heat exchanger and simulates its operating conditions by solving the thermal power balance on the tube-side (1), the thermal power balance on the shell-side (2), and by estimating the thermal power using the LMTD method (3).

$$Q = \dot{m}_{\text{hot}} \left(h_{\text{in,hot}} - h_{\text{out,hot}} \right), \tag{1}$$

$$Q = \dot{m}_{\text{cold}} \left(h_{\text{out,cold}} - h_{\text{in,cold}} \right), \tag{2}$$

$$Q = U A_{\text{HX}} F \cdot \text{LMTD}. \tag{3}$$

where $\dot{m}$ is the mass flow rate, h_{in} and h_{out} are inlet and outlet specific enthalpies respectively, U is the total heat transfer coefficient, A_{HX} is the heat transfer area, and F is the temperature correction factor.

The heat exchanger is designed following the TEMA standards that provide the correlations to estimate the heat exchanger geometry based on five geometrical parameters: the tube outside diameter (d_{o}), the number of shell passes (N_{sp}), the number of tube passes (N_{p}), the tube layout ($layout$), and the number of tubes (N_{t}). To select the optimal heat exchanger geometry, an internal optimisation has been built in the model considering a specific set of media, fluid-dependent constitutive relations for transport phenomena, constraints, and boundary conditions. Fig. 3 outlines the developed algorithm. Initially, the group of the possible combinations of design variables is identified. Then, each specific combination is selected and through the block *Design HX*, a specific heat exchanger design is proposed. This means that a heat transfer area, a detailed description of its geometry, the estimated investment cost, and the expected performances at the design point are provided. All the solutions corresponding to the combinations of design variables are grouped in an array. The model calculates the values of the ad-hoc defined objective function for the solutions and identifies the configuration that minimises/maximises the objective function. That configuration is proposed as the optimal heat exchanger configuration.

The block *Media* regards the fluids that flow in the shell-side and tube-side, and the heat exchanger material. The correlations as functions of temperature and pressure need to be defined for the main properties such as density, thermal conductivity, specific heat capacity, and dynamic viscosity. Additionally, the heat exchanger mass-specific cost should be provided. In the *Boundary Conditions*, the inlet/outlet fluid temperatures, operating pressures, and design thermal power should be set. The block *Fluid-dependent constitutive relations for transport phenomena* regards the correlations that should be defined ad-hoc for the fluids, e.g. the heat transfer and pressure losses correlations. Specific fluid-dependent variables can be user-defined. In *Constraints*, all the geometrical constraints to be considered in the design process should be specified, distinguishing:

1. volume constraints:
   - maximum heat exchanger length, and
   - maximum aspect ratio; and
2. velocity constraints:
   - maximum/minimum hot fluid velocity, and
   - maximum/minimum cold fluid velocity.

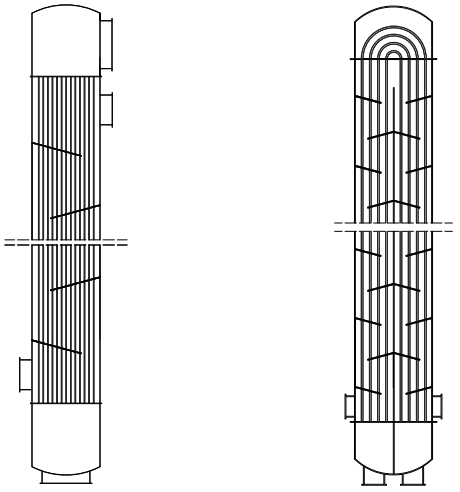

(a) 1:1 TEMA E STHE (b) 2:2 TEMA F STHE

Fig. 2. Heat exchanger configurations investigated.

Volume constraints are taken into account to fit the user requirements, while velocity constraints are needed for safety reasons. The velocity must be high enough to prevent any suspended solids from settling, but not that high to cause erosion (Sinnott, 1999). The *Objective Function* block should be customised to specify the goal of the heat exchanger optimisation, e.g. minimising the investment cost, or maximising the overall heat transfer coefficient. By default, the minimisation of the Total Annualised Cost (TAC) is utilised as an objective function (González-Gómez et al., 2018) in order to find a heat exchanger configuration that represents a good compromise between minimum investment cost and minimum operating cost. The TAC takes into account both capital and operation costs and it can be calculated as indicated in (4). CRF is the capital recovery factor and is defined in (5) adopting a real discount rate (f') during a lifetime (N_y) of 30 years. The real discount rate is calculated from (6) considering a nominal discount rate (f) equal to 7% (DOE, 2019) and an inflation rate (i) equal to 2.5% (DOE, 2019).

$$TAC = CRF \cdot C_{\text{inv}} + C_{\text{operating}} \tag{4}$$

$$CRF = \frac{f' \left(1 + f'\right)^{N_y}}{\left(1 + f'\right)^{N_y} - 1} \tag{5}$$

$$f' = \frac{1 + f}{1 + i} - 1 \tag{6}$$

The *Design HX* is the core block of the design strategy, where for a specific set of design variables, the heat exchanger design is fully characterised. Fig. 4 shows the procedure implemented in the Design HX block, which is explained in the following.

The procedure to define the heat exchanger design can be divided into the following steps: preliminary calculation, geometry definition, heat transfer coefficients calculation, pressure losses calculation, and costs estimation.

2.1. Heat exchanger preliminary calculations

According to the specific application, the following parameters need to be defined:

- Design thermal power (Q_{des});
- Hot-side inlet/outlet temperature ($T_{\text{in,hot}}/T_{\text{out,hot}}$);
- Hot-side inlet pressure ($p_{\text{in,hot}}$);
- Cold-side inlet/outlet temperature ($T_{\text{in,cold}}/T_{\text{out,cold}}$);
- Cold-side inlet pressure ($p_{\text{in,cold}}$).

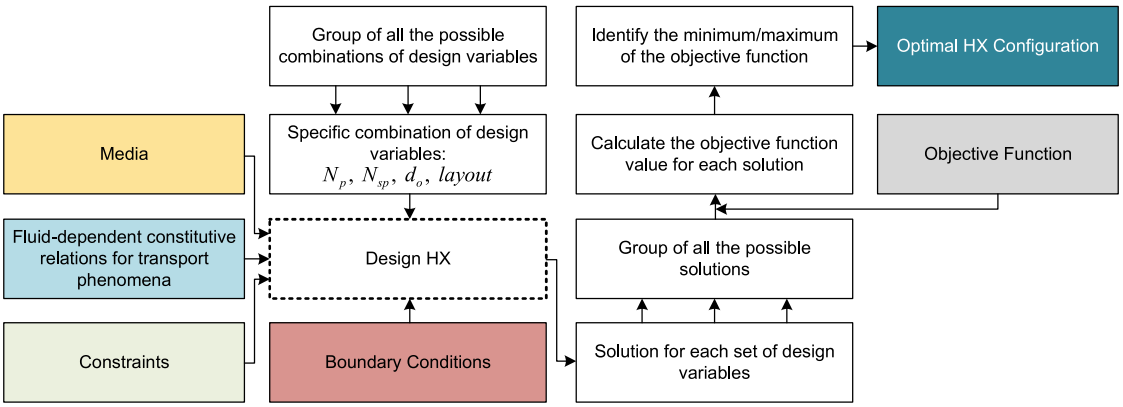

Fig. 3. Heat exchanger geometrical optimisation strategy.

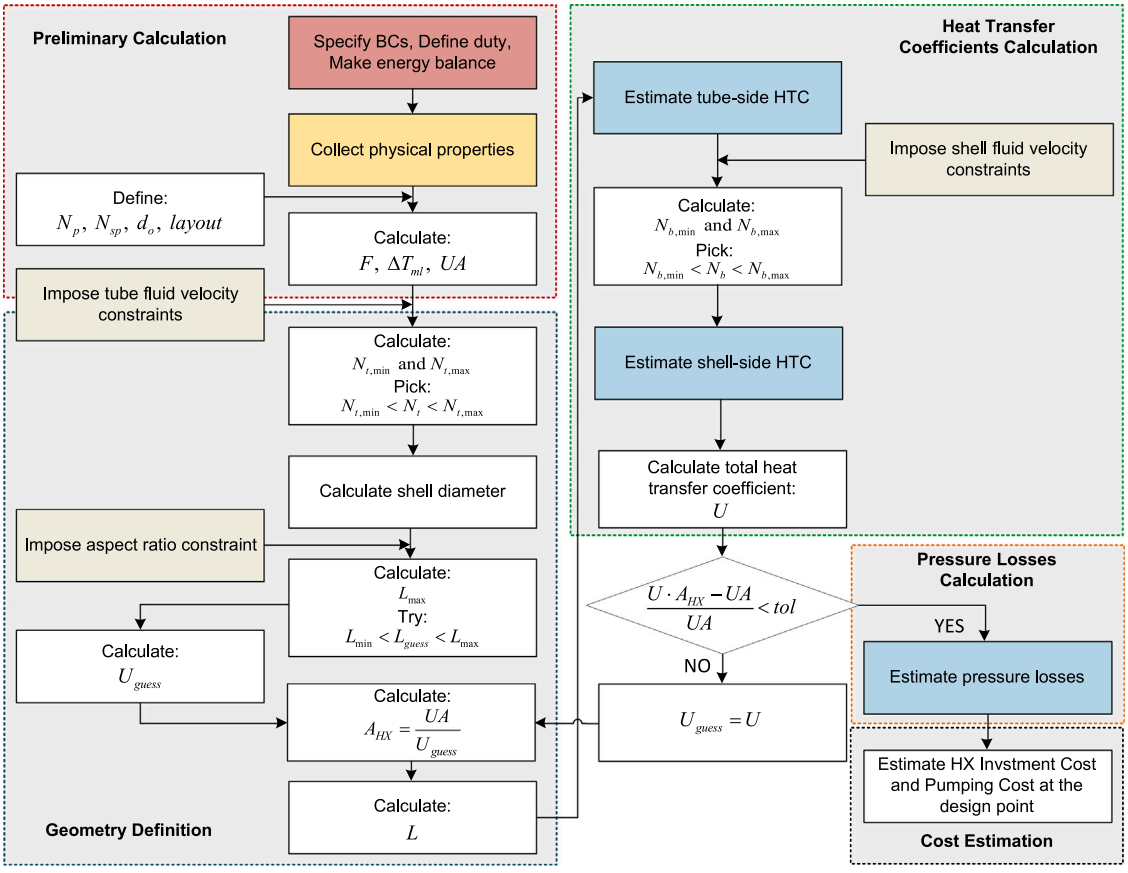

Fig. 4. Representation of the design strategy adopted in the *Design HX* block.

Based on the inlet/outlet temperatures mentioned above and on the media adopted, the inlet/outlet enthalpies can be calculated, as well as the average hot-side and cold-side temperatures. Then, the physical properties can be calculated at the average temperature for both sides, such as density (ρ), specific heat capacity (c_p), dynamic viscosity (μ), thermal conductivity (λ). Moreover, using the energy-balance Eqs. (1) and (2), the hot-side and cold-side mass flow rates can be calculated. Based on the inlet/outlet temperatures, the log-mean temperature difference (LMTD, ΔT_{LM}) can be calculated using (7).

$$\Delta T_{\mathrm{LM}} = \frac{\left(T_{\mathrm{out,hot}} - T_{\mathrm{in,cold}}\right) - \left(T_{\mathrm{in,hot}} - T_{\mathrm{out,cold}}\right)}{\ln\left(\frac{T_{\mathrm{out,hot}} - T_{\mathrm{in,cold}}}{T_{\mathrm{in,hot}} - T_{\mathrm{out,cold}}}\right)} \tag{7}$$

Then, the overall heat transfer coefficient is calculated as indicated in (8), re-writing Eq. (3).

$$U A_{\mathrm{req}} = \frac{Q}{F \cdot \Delta T_{\mathrm{LM}}} \tag{8}$$

where F is the temperature correction factor and is assumed to be equal to 1 as the one shell pass, one tube pass, and the two shell passes, two tube passes configurations can guarantee a counter-current flow arrangement (Thulukkanam, 2013). Although the overall heat transfer coefficient is calculated, the specific coefficients (U and A_{HX}) that give the required product need to be distinguished. This requires an iterative process.

2.2. Heat exchanger geometry

In this section, the heat exchanger geometry is defined considering the boundary conditions imposed in the previous section and respecting the volume and velocity constraints defined by the user. The number of tubes (N_t) is the design variable used to impose the tube side velocity constraints, (9). For a specific number of tube passes (N_p) and a fixed tube-side mass flow rate ($\dot{m}_{\mathrm{hot}}$), it is possible to determine the minimum and maximum acceptable number of tubes as functions of the maximum and minimum fluid velocity respectively:

$$N_{\mathrm{t,min}} = \frac{\dot{m}_{\mathrm{hot}} N_p}{\rho_{\mathrm{hot}} A_{\mathrm{cs}} v_{\mathrm{tube,max}}},\ N_{\mathrm{t,max}} = \frac{\dot{m}_{\mathrm{hot}} N_p}{\rho_{\mathrm{hot}} A_{\mathrm{cs}} v_{\mathrm{tube,min}}} \tag{9}$$

where A_{cs} is the single tube cross-section, ρ_{hot} is the tube-side fluid density, and v_{tube} is the tube-side fluid velocity. The number of tubes is picked between $N_{\mathrm{t,min}}$ and $N_{\mathrm{t,max}}$. For each value of the number of tubes in the acceptable range, a heat exchanger design is proposed, contributing to the group of all the possible solutions. Similar to what has been proposed for the other design variables, the optimal value is then selected through the internal optimisation shown in Fig. 3. Then, for a specific number of tubes, the shell inside diameter (D_S) is calculated as follow:

$$D_{\mathrm{s}} = d_o \left(\frac{N_t}{K_1}\right)^{1/n_1} + L_{\mathrm{bb}} + d_o \tag{10}$$

where L_{bb} and d_{o} are the bundle-to-shell clearance and the outer tube diameter, while K_1 and n_1 are the two constants function of the tube arrangement layout and the number of passes. For triangular layout and one tube pass K_1 and n_1 are equal to 0.319 and 2.142 respectively (Sinnott, 1999).

Successively, the heat exchanger length guess-value (L_{guess}) is picked between the minimum (L_{min}) and the maximum acceptable length (L_{max}). These boundary values can be user-defined or calculated based on the maximum aspect ratio. The recommended tube length to shell diameter aspect ratio is in the range of 5 to 10 (Fanaritis and Bevevino, 1976). Thus, if no particular volume constraints are defined, the maximum acceptable heat exchanger length is calculated imposing a maximum aspect ratio equal to 10. The guess-value of the total heat transfer coefficient (U_{guess}) is calculated as follow:

$$U_{\mathrm{guess}} = \frac{U A_{\mathrm{req}}}{A_{\mathrm{guess}}} \tag{11}$$

During the iterative procedure, the heat exchanger length (L) is calculated by rewriting Eq. (11) and adopting the calculated value of the total heat transfer coefficient.

The number of baffles is used to impose the shell-side velocity constraints, though the baffle spacing. For a fixed tube bundle geometry (d_o, N_t, L, $layout$, N_p, N_{sp}) and a fixed shell-side mass flow rate ($\dot{m}_{\mathrm{cold}}$), it is possible to determine the minimum and maximum acceptable number of baffles as a function of the maximum and minimum shell-side fluid velocity. (12) show the minimum and maximum number of baffle as a function of the maximum ($l_{\mathrm{b,max}}$), the minimum ($l_{\mathrm{b,min}}$) baffle spacing, the baffle thickness (t_{baffle}), and the tube sheet thickness (L_b). Then, the maximum and minimum baffle spacing are linked to the minimum ($v_{\mathrm{shell,min}}$) and maximum shell-side fluid velocity ($v_{\mathrm{shell,max}}$) respectively, as shown in (13).

$$N_{\mathrm{b,min(max)}} = \frac{L - t_{\mathrm{baffle}} + 2 \cdot L_b}{l_{\mathrm{b,max(min)}} + t_{\mathrm{baffle}}} - 1 \tag{12}$$

$$l_{\mathrm{b,max(min)}} = \frac{N_{\mathrm{sp}} \cdot \dot{m}_{\mathrm{cold}}}{\rho_{\mathrm{cold}} \cdot L_{\mathrm{cf}} \cdot v_{\mathrm{shell,min(max)}}} \tag{13}$$

where ρ_{cold} is the shell-side fluid density, and L_{cf} the crossflow free length. The number of baffles is picked between $N_{\mathrm{b,min}}$ and $N_{\mathrm{b,max}}$ to minimise the difference between the target $U A_{\mathrm{req}}$ and the calculated product $U \cdot A_{\mathrm{HX}}$. For a specific number of baffles, the baffle thickness and the baffle spacing are calculated iteratively. The rest of the parameters that characterise the heat exchanger geometry are calculated as shown in Appendix A, Table A.1.

Table 1
Summary of the design parameters of the reference case CSP system.

Variable	Value	Unit
Solar field size	976500	m^2
Design optical efficiency field	65	%
Receiver thermal design power	543	MW
Tower Height	150	m
Storage hours	12	h
Solar Multiple (SM)	2.5	–
Power block net power	100	MW_e
Design power block gross efficiency	51	%
Turbine inlet temperature	700	°C
Design ambient temperature-cooling	30	°C
Design net-to-gross efficiency	90	%
Generator efficiency	98.7	%

2.3. Heat transfer coefficients

The total heat transfer coefficient is evaluated as a function of the shell-side (h_{s}) and tube-side (h_{t}) heat transfer coefficients as shown in (14).

$$U = \left(\frac{1}{h_s} + R_s + \frac{1}{h_t} \cdot \frac{d_o}{d_i} + \frac{d_o \ln\left(d_o/d_i\right)}{2\lambda_{\mathrm{wall}}}\right)^{-1} \tag{14}$$

where R_{s} is the fouling resistance that can be user-defined according to the fluid utilised, d_{i} is the tube inner diameter, and λ_{wall} is the thermal conductivity of the wall function of the material selected for the heat exchanger.

The shell-side heat transfer coefficient is estimated using the Bell-Delaware method, the most widely recognised standard for the design of heat exchangers (Bott et al., 1994). This method estimates the shell-side heat transfer coefficient calculating first the ideal heat transfer coefficient ($h_{\mathrm{s,id}}$) and applying successively three correction factors. The ideal heat transfer coefficient assumes complete crossflow between the fluid in the shell-side and tube bundle, to which corrections are applied considering the following effects:

- the baffle cut and spacing. This correction factor is used to take into account that only a fraction of the tubes are in pure cross-flow (J_C);
- flow leakage due to shell-to-baffle and tube-to-baffle clearances (J_L);
- bundle bypass flow due to the gap between tube bundle and shell (J_B).

The resulting shell-side heat transfer coefficient is calculated as the product between the ideal heat transfer coefficient (HTC) and the correction factor as shown in Eq. (15). The ideal heat transfer coefficient and the three correction factors can be calculated as presented in Table A.5, in Appendix A.

$$h_{\mathrm{s}} = h_{\mathrm{s,id}} \cdot J_C \cdot J_L \cdot J_B \tag{15}$$

The tube side heat transfer coefficient is calculated as a function of the dimensionless Nusselt number (Nu_{hot}). Since the hot-fluid flows inside a pipe, several correlations available in literature can be utilised to estimate the dimensionless Nusselt number as a function of two dimensionless numbers: Reynolds (Re_{hot}) and Prandtl (Pr_{hot}). According to the fluid utilised, the user should define the most suitable correlation for which the average temperature between inlet and outlet can be used.

2.4. Pressure drops

The shell-side pressure drop is estimated using the Bell-Delaware method, one of the most realistic methods counting for the bypass and leakage streams caused by the baffles (Shweta et al., 2014). The shell-side pressure drop (Δp_s) consists of the sum of the pressure drop due

Table 2
Cost assumptions for the CSP plant.

Variable	Value	Unit	Reference
Heliostat field	75	USD/m^2	DOE (2019), Mehos et al. (2016)
Site improvement	10	USD/m^2	Mehos et al. (2016)
Tower reference cost	7.613	MUSD	Turchi et al. (2019)
Tower cost exponent	0.0113	–	Turchi et al. (2019)
Receiver reference cost	105.1	MUSD	*
Receiver reference area	1571	m^2	Turchi et al. (2019)
Receiver cost exponent	0.7	–	Turchi et al. (2019)
Storage	40	USD/kWh$_{th}$	DOE (2019)
Power block	900	USD/kW$_e$	DOE (2019)
Balance of Plant	250	USD/kW$_e$	Turchi et al. (2019)
Contingency	10	% direct costs	DOE (2019)
EPC	9	% direct costs	DOE (2019)
Land	2.47	USD/m^2	DOE (2019), Mehos et al. (2016)
Fixed O&M cost — cap	40	USD/kW – yr	DOE (2019), Mehos et al. (2016)
Variable O&M cost — gen	3	USD/MWh – yr	DOE (2019)

* Adapted from Turchi et al. (2019) to fit a real quote.

Table 3
Sodium–chloride salt heat exchanger design assumptions for the reference case.

Variable	Value	Unit of measure
Thermal design power	543	MW
Hot/Cold Na temperatures	740/540	°C
Hot/Cold CS temperatures	720/520	°C
Material	Haynes230	–
Specific material cost	84	USD/kg
Tube-side velocity limits	1.2–2.4 (Fous, 1972)	m/s
Shell-side velocity limits	0.5 (González-Gómez et al., 2018)–1.5 (Sinnott, 1999)	m/s

Table 4
Heat exchanger geometrical design variables.

Variable	Symbol	Assumed range
Tube outside diameter	d_o	[6.35–63.5 mm]
Number of tube passes	N_p	[1, 2]
Number of shell passes	N_{sp}	[1, 2]
Tube layout	$layout$	$[triangular, square]$
Number of tubes	N_t	$[N_{t,min}, N_{t,max}]$

to crossflow (Δp_c), window region (Δp_w), and entrance and exit regions (Δp_e) (Bell, 1988) as presented in (16).

$$\Delta p_s = \Delta p_c + \Delta p_w \cdot N_b \cdot R_L + \Delta p_e \tag{16}$$

where R_L is the correction factor for baffle leakage effects for pressure drop. The calculations of each pressure losses contribution are available in Table A.4 in Appendix A.

The tube-side pressure drop is estimated by adopting Frank's method. This method considers the friction loss in the tubes and the pressure drop due to geometry discontinuities that the fluid faces through the tube bundle. In detail, Frank's method recommends a velocity head per pass value equal to 2.5 as the most realistic value to use (Sinnott, 1999). The pressure drop is calculated using (17):

$$\Delta p_t = N_p \cdot \left(8 \cdot j_f \frac{L}{d_i}\left(\frac{\mu_{hot,bulk}}{\mu_{hot,wall}}\right)^{-m} + 2.5\right) \cdot \frac{\rho_{hot} \cdot v_{tube}^2}{2} \tag{17}$$

where the dimensionless friction factor and the exponent assume different values for laminar and turbulent flow as shown in Table A.3, in Appendix A (Sinnott, 1999).

2.5. Capital and operating costs

This section presents the heat exchanger investment cost and operating costs functions implemented in the heat exchanger model. Two complementary approaches are adopted for the heat exchanger investment cost. The first relies on the methodology proposed by Turton et al. (2012), which is based on a survey of equipment manufacturers to calculate the purchased cost of conventional equipment types typically utilised in chemical processes. This method is available in Table A.2, in Appendix A. Although it is widely adopted in literature, it can be applied only if the heat exchanger area ranges between 10 and 1000 m^2.

To overcome the applicability limits of the Turton approach, a second cost function was developed by the authors. The investment cost is a function of the heat transfer area and it respects the economy of scale: the investment cost as a function of the heat transfer area is concave downward. The investment cost is shown in (18) as a function of the mass-specific material cost ($c_{material}$), the manufacturing factor (F_{ma}), and a mass-over-area factor (M_a). The mass-specific material cost is the bare material cost per kilogram, and it needs to be user-defined according to the selected HX material. The mass over area factor is assumed equal to 9.6 kg/m^2 according to the average heat exchanger mass over area value for the assumed tube diameter range. The manufacturing factor is a correction factor to convert the bare material cost into the equipment specific cost (19). This factor is assumed to be a function of the heat transfer area and tends asymptotically to F_{min}. The minimum manufacture factor is assumed to equal 1.65 according to experts from the University of South Australia.

$$C_{inv} = c_{material} \cdot F_{ma} \cdot M_a \cdot A_{HX} \tag{18}$$

$$F_{ma} = F_{min} + c \cdot A_{HX}^{-m} \tag{19}$$

where the two constants c and m need to be found using two known cost values for two heat transfer areas. To respect the economy scale, the exponent m needs to be between 0 and 1, and the constant c needs to be larger then 0.

The pumping cost (C_{pump}) is assumed the only heat exchanger annual cost and it is calculated using (20). It has been assumed an annual operating time (tm_y) of 4500 hours/year, electricity cost (c_{power})

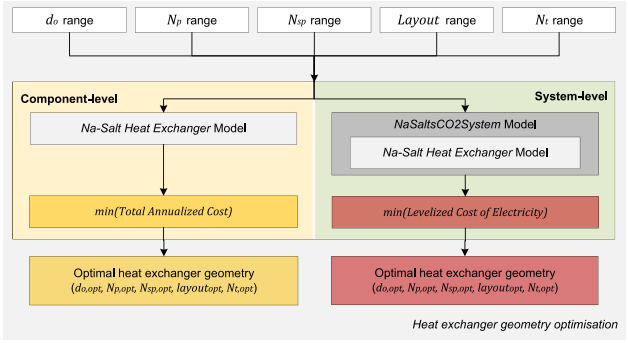

Fig. 5. Flowchart of the heat exchanger geometry optimisation (component-level and system-level).

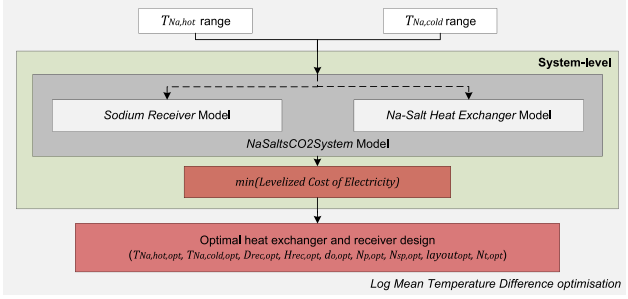

Fig. 6. Flowchart of the log-mean temperature difference (system-level).

of 0.14 USD/kWhe, and pump efficiency (η_{pump}) of 70% (González-Gómez et al., 2018). These values are assumed as starting points and fine-tuning is required based on the particular application.

$$C_{pump} = c_{power} \cdot \frac{tm_y}{\eta_{pump}} \cdot \left(\frac{\dot{m}_{cold} \cdot \Delta p_s}{\rho_{cold}} + \frac{\dot{m}_{hot} \cdot \Delta p_t}{\rho_{hot}} \right) \tag{20}$$

3. System model reference case

The sodium-salt-sCO_2 CSP system model *Na-Salt-sCO2-System* proposed in this paper was developed by using the Modelica programming language, building on components in the *SolarTherm* framework (Scott et al., 2017). The system configuration selected as a reference case is a 100 MW_e CSP plant located in Daggett, CA, USA. The capacities of the principal system components and the most relevant design parameters are summarised in Table 1. Liquid sodium is used as heat transfer fluid in the receiver, allowing receiver operating temperatures of 520 °C to 740 °C, and a novel ternary eutectic chloride salts is adopted as storage fluid in a two-tank indirect system. The advanced chloride salts are stored at 720 °C in the hot tank, and 500 °C in the cold tank. The sCO_2 turbine inlet temperature (TIT) is equal to 700 °C. The CSP plant annual energy performances and the techno-economic KPI values such as the LCOE, the Energy Per Year (EPY), and the CF were estimated. The EPY is calculated as the sum of the annual net electricity produced. The CF is estimated by dividing the total energy produced in a year by the amount of energy it would have produced if it ran at full output over that year. The LCOE is calculated as reported in (21):

$$\text{LCOE} = \frac{\text{CAPEX} \cdot \text{CRF} + \text{OPEX}}{\text{EPY}} \tag{21}$$

where CAPEX and OPEX are the total capital cost and the annual operating cost of the plant respectively. Table 2 summarises the cost assumptions for the main components identified in the plant. The considered cost functions are reported in Table B.1, in Appendix B. A plant operational lifetime of 30 years has been considered for plant (Wang et al., 2021).

3.1. Sodium receiver

The sodium receiver design consists of planar banks with parallel thin-walled pipes stacked between two headers, with the banks forming pseudo-cylindrical configurations. The liquid sodium flows through the receiver pipes via flow-paths that are defined considering the sodium velocity restrictions. The flow paths design and panel pipes diameter were determined for different design temperatures by trade-offing between receiver efficiency and design simplicity while keeping the incident flux below allowable flux densities (AFD) (See Fig. B.1 in Appendix B) (Wang et al., 2021; Asselineau et al., 2020). AFDs were estimated using inelastic design guidelines from Argonne National Laboratories to define aggressive best-estimate limits for a 30 year lifetime of the receiver (Barua et al., 2020). The AFD calculation assumed a simple 10 hour design cycle and a steady-state thermal model without significant transients. Stress and strain intensities were determined using a 2D generalised plane strain finite element analysis at a single-equinox solar-noon design point (Logie et al., 2018). The design cycle was repeated for five years to obtain sufficient relaxation, allowing lives of up to 30 years to be projected without creep-fatigue or thermal ratchet.

For a specific design proposed, the design and off-design receiver thermal efficiency (η_{rec}) can be estimated as a function of the incident power (Q_{field}) and of the ambient temperature (T_{amb}), as shown in (22). The polynomial equations are updated based on the receiver design performing a least-squares regression from off-design data points obtained from simulations with a detailed heat transfer model (Asselineau et al., 2020). The off-design performance of the sodium receiver can be calculated by solving the energy balance reported in (23).

$$\eta_{rec} = A_0 \cdot \log_{10}\left(T_{amb}\right) + \sum_{k=0}^{3} C_k \left[\log_{10}\left(\dot{Q}_{field}\right)\right]^k \tag{22}$$

$$\alpha_{eff} \cdot Q_{field} \cdot \eta_{rec} = \dot{m}_{rec} \cdot \left(h_{rec,out} - h_{rec,in}\right) \tag{23}$$

where α_{eff} is the absorption coefficient, $\dot{m}_{rec}$ is the sodium mass flow rate, $h_{rec,out}$ and $h_{rec,in}$ are the outlet and inlet sodium enthalpies.

3.2. Power block

The power block was modelled interpolating the performance estimated by the sCO_2 Cycle Integration macro available in System Advisor Model (SAM), v14.02.2020. The design point is characterised by the TIT, the nominal gross power ($P_{gross,des}$), the nominal inlet thermal power ($Q_{flow,des}$), the design cooling power ($W_{cool,des}$), and the design ambient temperature ($T_{amb,des}$). The off-design performance was evaluated by means of three coefficients (k_w, v_w, and k_q), which are obtained at every time steps as functions of the load, the ambient temperature, and the chloride salt inlet temperature (see Table B.2 in Appendix B). The gross electric power produced (W_{gross}) and the cooling power required ($W_{cooling}$) are calculated using (24) and (24) respectively. For a given chloride salt mass flow rate (m_{flow}) and inlet enthalpy value (h_{in}), the returning chloride salt enthalpy (h_{out}) is calculated by using (26). Then, the net electric power produced (W_{net}) is evaluated as shown in (27).

$$W_{gross} = k_w \cdot P_{gross,des} \tag{24}$$

$$W_{cooling} = v_w \cdot W_{cool,des} \tag{25}$$

$$m_{flow} \cdot (h_{in} - h_{out}) = k_q \cdot Q_{flow,des} \tag{26}$$

$$W_{net} = W_{gross} - W_{par} - W_{cooling} \tag{27}$$

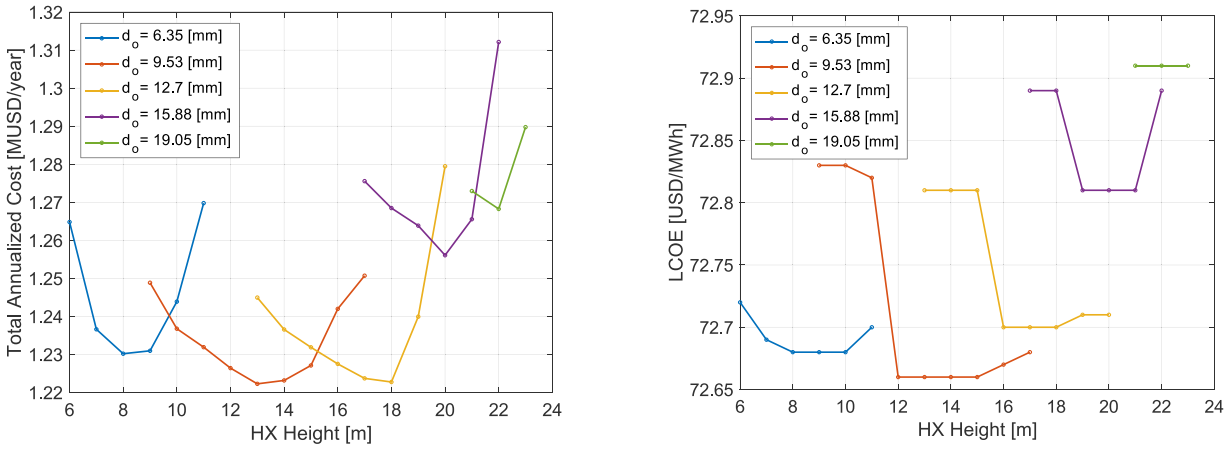

(a) Total Annualized Cost (TAC)

(b) Levelized Cost of Electricity (LCOE)

Fig. 7. KPIs function of the tube outside diameter (d_o) and tube pass length (L).

where W_{par} is the power required to cover the parasitic losses. The power block efficiency (η_{PB}) is calculated as the ratio between the net electric power produced and the input thermal power.

3.3. Sodium-chloride salt heat exchanger

Based on the design parameters of the CSP reference case, the heat exchanger model presented in Section 2 is characterised as a sodium-chloride salt heat exchanger. For safety precautions and to reduce thermal losses, sodium was placed on the tube side, while the chloride salt was on the shell side. The design thermal power was set equal to the receiver design power. Also, the heat exchanger design temperatures were identified based on receiver and storage design conditions. The heat exchanger material is selected according to the fluids considered, taking into account corrosion issues and maximum allowable stress in the temperature range of this application. According to Armijo (2019), Haynes230 (H230) is the recommended material for the hot side of the CSP plant because it presents the minimum corrosion rate and the maximum allowable stress in the temperature range of 700 °C to 750 °C. Finally, to customise the heat exchanger model, the tube side heat transfer coefficient correlation was adopted according to Benoit et al. (2016). The recommended correlation for liquid sodium in tubes is presented in (28) as a function of the Peclet non-dimensional number (Pe):

$$Nu = A + 0.018 \cdot Pe^{0.8} \tag{28}$$

with:

$$A = \begin{cases} 4.5 & \text{when } Pe \leq 1000 \\ 5.4 - 9 \times 10^{-4} \cdot Pe & \text{when } 1000 < Pe \leq 2000 \\ 3.6 & \text{when } Pe > 2000 \end{cases} \tag{29}$$

Table 3 summarises the design assumptions for the specific sodium-chloride salt heat exchanger included in the reference case CSP plant. By employing the customised heat exchanger model in the *NaSaltsCO2System*, the sodium-salt heat exchanger was designed aiming at minimising the LCOE, providing a complete geometry description, and an estimation of the performances and costs.

4. Methodology

As a first step in the study, the most suitable heat exchanger design for the reference case CSP plant is identified. Two different approaches are implemented: component-level and system-level optimisations as

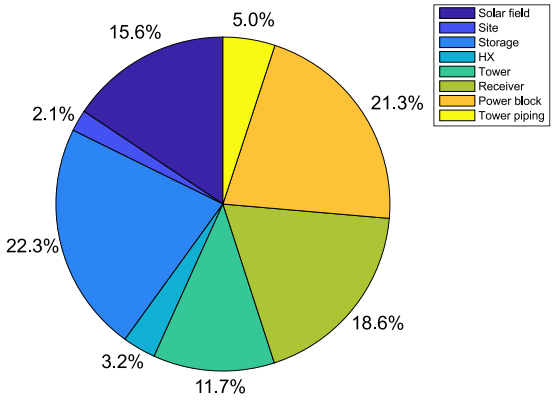

Fig. 8. CSP system cost breakdown.

shown in the flowchart in Fig. 5. Firstly, the design variables, such as number of tubes, tube outside diameters, tube layout, number of shell passes, and number of tube passes are optimised to minimise the TAC. Successively, the heat exchanger configuration that minimises the LCOE of the CSP plant is identified (system-level optimisation). The assumed range of the design variables are based on TEMA standards and are presented in Table 4. Besides the number of tubes, for which the assumed range is calculated based on the maximum/minimum velocity in the tube side, the other four parameters are provided in the model as arrays of suggested values. The tube outside diameter range is assumed according to TEMA dimensional data for commercial tubing (Drake and Carp, 1960). The ranges of the number of tube and shell passes are assumed based on the configuration included in the heat exchanger model. For the tube layout, the most common tube arrangements in shell and tube heat exchanger are assumed (Drake and Carp, 1960).

As a second step, the optimisation of the LMTD is proposed. This investigation aims to highlight the potential reduction of the LCOE of the CSP plant that can be achieved by acting on the LMTD of the heat exchanger. Fig. 6 shows a flowchart of this system-level optimisation. The analysis is carried out on the combined receiver-heat exchanger block by varying the sodium-side temperatures of the LMTD. On the salt side, the nominal temperatures of 500 °C to 720 °C are preserved. The reference case is slightly modified, optimising the receiver capacity. The impact of the sodium temperatures on the CSP system

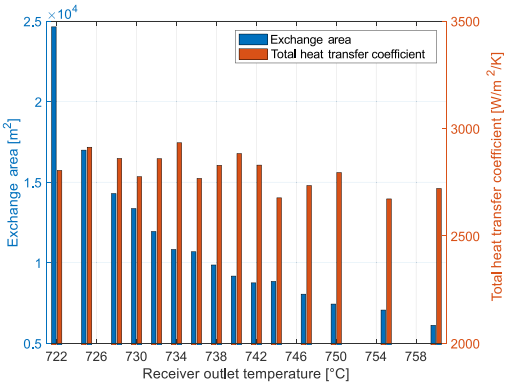

(a) Exchange area and total heat transfer coefficient

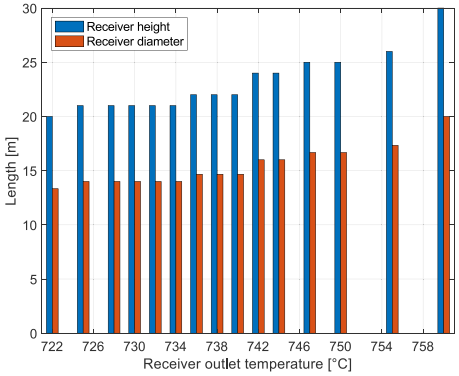

(b) Height and diameter of the receiver

Fig. 9. HX and receiver design variables as a function of the receiver outlet temperature (Fixed inlet–outlet temperature).

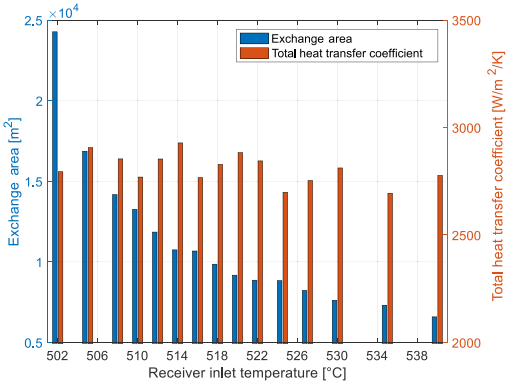

(a) Exchange area and total heat transfer coefficient

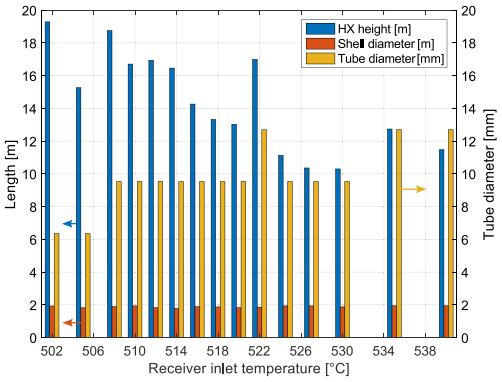

(b) Height, shell diameter, and tube diameter

Fig. 10. HX design variables as a function of the receiver inlet temperature (Variable inlet–outlet temperature).

performances is analysed assuming two approaches: fixed inlet–outlet temperature change and variable inlet–outlet temperature change. In detail, the fixed inlet–outlet temperature change is chosen equal to 220 °C (reference case) and the receiver outlet temperature ranges between 722 °C and 760 °C. For the variable inlet–outlet temperature approach, the maximum sodium temperature was fixed equal to 740 °C, and the receiver inlet temperature was varied between 502 °C and 540 °C.

In the end, a sensitivity analysis on the heat exchanger cost is proposed aiming to show its impact on the total plant cost and the LCOE. Thus, assuming the reference case CSP plant configuration, the heat exchanger cost was modified by varying the heat exchanger mass-specific material cost (c_{H230}) from half to three times the reference cost value.

5. Results

In this section, the main results are presented. Firstly, a design of the sodium-chloride heat exchanger is proposed for the reference case CSP plant. The influence of some geometrical parameters on the heat exchanger design definition and the LCOE of the CSP plant is shown. Furthermore, the impact of the log-mean temperature difference on the system performance and a sensitivity analysis of the cost of the heat exchanger are analysed.

5.1. Optimisation of HX internal configuration

The heat exchanger configuration that minimised the TAC is achieved for a heat exchanger length equal to 13 m and a tube outside diameter (d_o) of 9.53 mm as shown in Fig. 7(a). A triangular pitch and a single shell pass/single tube pass configuration were adopted since they lead to lower TAC values compared to square pitch and the two shell passes/two tube passes configuration. Fig. 7(b) shows the LCOE as a function of the same design variables adopted in Fig. 7(a). The heat exchanger configuration that minimises the TAC coincides with the heat exchanger configuration that minimises the LCOE. It is possible to assess that the design that minimises the TAC represents a good guess of the configuration that minimises the LCOE. In line with this result, from this point onward, the HX configuration will be defined through the model internal optimisation for all the rest of the system-level optimisations conducted.

The design parameters of the most suitable heat exchanger for the reference case CSP plant are provided in Table 5. This shell and tube heat exchanger design leads to a LCOE value equal to 72.7 USD/MWh. The annual energy performances and costs were estimated by using the developed `NaSaltsCO2System` model. The Energy Per Year (EPY) amounts to 560 GWh, and a capacity factor (CF) of 64% was calculated. Fig. 8 shows the plant direct costs breakdown, where the sodium-salt HX represents the 3.2%.

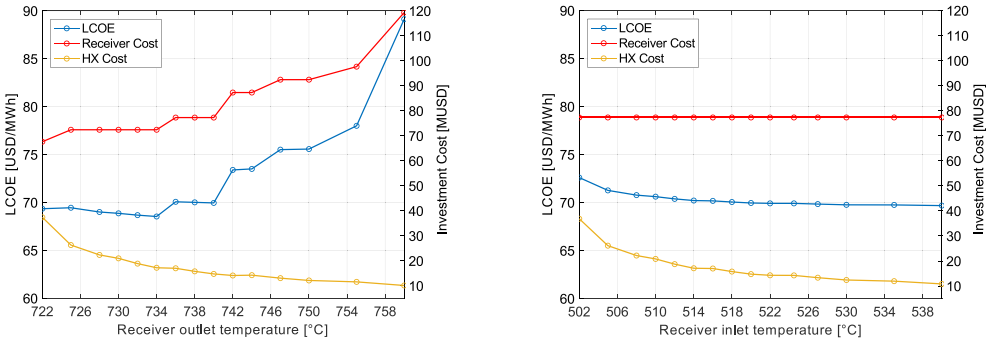

(a) Fixed inlet-outlet temperature change approach.

(b) Variable inlet-outlet temperature change approach.

Fig. 11. Levelized Cost of Electricity and receiver and HX investment costs as function of the receiver design temperatures.

Table 5
Summary of most relevant HX variables.

Variable	Value	Unit of measure
Design thermal power	543	MW
Heat transfer area	9400	m^2
Tube length	13	m
Overall height	15	m
Shell diameter	1.83	m
Total heat transfer coefficient	2900	W/m^2K
Number of tubes	23500	–
Tube outside diameter	9.53	mm
Tube arrangement	Triangular	–
Number of baffles	3	–
Baffle tilt angle	15	°
Design sodium velocity	1.9	m/s
Design chloride-salt velocity	1.5	m/s
Investment cost	15	M · USD
Design annual pumping cost	240	k · USD

5.2. LTMD optimisation

The variation of the sodium temperatures affects both the heat exchanger and the receiver design. As for the heat exchanger, in comparison to the reference case, keeping the same thermal design power, a larger LMTD implies a more compact heat exchanger design. On the other side, for what concerns the receiver, assuming a fixed solar field size, the maximum allowable flux that the receiver material can withstand is a function of the receiver area and operating temperatures. Hence, by increasing the sodium temperatures, the receiver dimensions need to increase as well to preserve the maximum allowable flux. Moreover, larger receivers lead also to higher thermal losses and consequently lower thermal efficiencies. Fig. 9 shows the variations of the heat exchanger area 9(a) and the receiver dimensions 9(b) as a function of the receiver outlet temperature. As for the receiver, Fig. 9(b) shows that when the receiver outlet temperature varies from 722 °C to 760 °C both the diameter and the height of the receiver increase proportionally. For what concerns the heat exchanger, compared to the reference case, reducing the LMTD the exchange area (A) increases to fit the design thermal power. Fig. 9(a) shows also that the total heat transfer coefficient (U) is almost preserved while reducing the LMTD. Consequently, the overall heat transfer coefficient (UA) increases driven by the exchange area variation.

In the variable inlet–outlet temperature change approach, the receiver design is unaffected because the maximum sodium temperature is kept constant. Consequently, only the heat exchanger design is modified by varying the receiver inlet temperature. Fig. 10(a) shows that the increase in LMTD is compensated by a reduction of the UA value. In detail, the heat exchanger area decreases increasing the receiver inlet temperature, while the total heat transfer coefficient is preserved. Fig. 10(b) shows that the reduction of the heat transfer area is obtained by reducing the heat exchanger length while increasing the tube outside diameters. Consequently, the number of tubes decreases. The tube outside diameters increase with the receiver inlet temperature to fit the velocity constraints and to minimise the TAC of the heat exchanger.

A comparison of the two adopted approaches is shown in Fig. 11. Figs. 11(a) and 11(b) show the plant LCOE, the investment costs for the receiver and the heat exchanger respectively for the fixed and the variable inlet–outlet temperature change approaches. Fig. 11(a) shows that the minimum LCOE value is equal to 68.5 USD/MWh and it is obtained adopting inlet and outlet sodium temperatures of 514 °C and 734 °C. Thus, by reducing the LMTD from 20 °C (reference case) to 14 °C, the receiver investment cost decreases whereas the heat exchanger cost increases. Since the receiver cost constitutes a larger share of the total capital cost, a cheaper receiver and a more expensive heat exchanger minimised the plant LCOE. In contrast, Fig. 11(b) shows that increasing the LMTD, the LCOE decreases due to the reduction of the heat exchanger cost with a fixed receiver design. The minimum LCOE is 69.7 USD/MWh and is obtained for the maximum receiver inlet temperature considered.

5.3. Analysis sensitivity to HX investment cost

By varying the normalised material specific cost from 0.5 to 3, the share of the heat exchanger cost on the total plant investment cost ranged from 2% to 9%. Fig. 12(a) shows that the HX investment cost increased piecewise linearly with the normalised material specific cost. Accordingly, the LCOE varied with a similar trend from 71.9 to 76.2 USD/MWh. The changes in slope that can be noticed between 0.9 and 1, and between 1.6 and 1.7 were due to the change in the number of tubes and height of the heat exchanger as shown in Fig. 12(b). Indeed, for each cost value, a different heat exchanger design was proposed through the internal optimisation implemented in the heat exchanger model. For high material costs, the internal optimisation led to designs characterised by a small exchange area and a large total heat transfer coefficient. This was driven by a reduction in the number of tubes, and a simultaneous increase in the tube pass length as shown in Fig. 12(b). Additionally, Fig. 12(b) shows that the tube outside diameter was preserved.

Therefore, by increasing the material cost, the heat exchanger internal optimisation tool prioritised the configurations that minimise the investment cost rather than looking for a compromise between heat exchanger investment cost and operating costs.

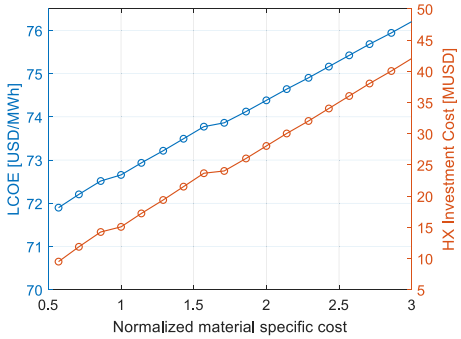

(a) Levelized Cost of Electricity and HX investment cost.

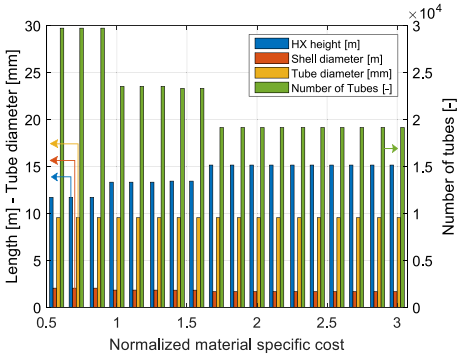

(b) Tube outside diameter, shell diameter, tube pass length, and the number of tubes.

Fig. 12. KPI, cost, and geometry of the HX as a function of the normalised material specific cost.

6. Discussion

In this work, the developed shell and tube heat exchanger model was customised to design the most suitable sodium-salt heat exchanger for a sodium-salt-sCO_2 CSP system located in Daggett, USA. A base-case LCOE of 72.7 USD/MWh was estimated for a CSP plant characterised by a receiver capacity of 543 MW_{th}, 12 h of TES, and a 100 MW_e power block. The most suitable HX design was shown to be a single-shell/single-tube pass configuration, with vertical alignment, characterised by an overall height of 15 m, and a shell diameter of 1.8 m. The very high aspect ratio and the proposed tube diameter (9.53 mm) are in agreement with Drake and Carp (1960), who found this same diameter gives the best balance of HX economics and performance. The main observations on the results obtained, and possible improvements, are explained below:

- The developed HX model is a promising tool for designing and simulating the operations of shall-and-tube heat exchangers. Throughout the optimisations and investigations conducted, it was found to be a robust, stable, and flexible model that provides the design geometry and annual performances estimations for different CSP plant configurations and operating conditions. The quasi-static assumption may be relaxed in future works to investigate the influence of switch on/off dynamics on the annual performance of the HX. Moreover, switching from a lumped-parameter to a one-dimensional model could lead to different performance estimates and different design selection criteria accounting for thermal-stress issues.
- Regarding the definition of the HX internal geometry, a comparison between the component-level and the system-level optimisation indicated that the HX configuration that minimised the TAC was a good guess for the design that minimised the LCOE of the sodium-salt-sCO_2 CSP system. Therefore, the TAC approach turned out to be advantageous and allows to save computational time during optimisations and sensitivity analyses. However, a variation in the cost assumptions, in the system performance, in the scale of the plant may lead to different scenarios, where the HX would cover a higher share of the overall cost with a higher impact on the LCOE of the plant. The sensitivity analysis on the material cost pointed out that, by increasing the HX material cost, the TAC approach selects the HX design that minimises the investment cost, mitigating the impact on the plant LCOE. By doubling the HX investment cost, the plant LCOE increased from 72.7 to 74.4 USD/MWh.
- The optimisation with the largest impact on the LCOE was the investigation regarding the LMTD of the HX conducted on the combined receiver-heat exchanger block. Reducing the receiver size at the expense of a larger and more expensive HX leads to lower LCOE, without a significant impact on the plant performance. In particular, by adopting a maximum receiver operating temperature equal to 734 °C, the LCOE was reduced to 68.5 USD/MWh, guaranteeing suitable temperature levels on the chloride-salt side. Besides, by keeping the output sodium receiver temperature (740 °C) and varying the inlet one from 520 °C to 540 °C, the receiver configuration is preserved while the HX area decreases, without significant reduction of the energy performances. This results in lower LCOE values. Future work needs to be conducted to further explore the impact on the HX and receiver design for higher inlet sodium temperatures and also varying the salt-side temperatures. The impact of the LMTD variation may foster additional LCOE reductions on the global CSP system.

7. Conclusions

In this work, a sodium-to-chloride salt heat exchanger for advanced, high-temperature CSP applications was proposed. A quasi-static thermodynamic model of the heat exchanger was developed implementing TEMA standards coupled with literature guidelines. This novel open-source heat exchanger model was developed as a reusable and general model for shell and tube heat exchangers, with the possibility of being customised in terms of HTF, volume and velocity constraints, boundary conditions, and heat transfer correlations.

The model was incorporated into a newly-developed sodium–salt–sCO_2 CSP system model. The base-case design had a receiver and a heat exchanger capacity of 543 MW_{th}, 12 h of TES, and a 100 MW_e power block. The sodium–salt heat exchanger was designed with the aim of minimising the system LCOE. The most cost-effective HX design had a 15 m shell and tube heat exchanger arranged vertically with a single shell pass, a single tube pass, and a height-to-diameter ratio of 8.0. The resulting LCOE and the CF of the plant were equal to 72.7 USD/MWh and 64%, respectively; the cost of the resulting heat exchanger was equal to 3.2% of the system total capital cost. During several investigations carried out in this work, the heat exchanger model proved its flexibility, robustness, and versatility, providing a complete geometry description, and an estimation of the performance and cost for different boundary conditions and techno-economic assumptions.

The system-level optimisation carried out on the receiver-heat exchanger block highlighted that reducing the receiver size at the expense

of larger and more expensive heat exchangers leads to lower LCOEs without a significant impact on the plant performance. The minimum LCOE equal to 68.5 USD/MWh is found for a sodium receiver outlet temperature equal to 734 °C, keeping both the cold sodium temperature and the salt-side temperatures unchanged. Furthermore, varying the inlet sodium receiver temperature from 520 °C to 540 °C, it was shown that the receiver design is unchanged while the heat exchanger area decreases, without significant reduction of the energy performance. This results in lower LCOE values. Further improvements and consequential LCOE reduction can be achieved by investigating the influence of the salt-side temperature on the heat exchanger and the CSP system design.

The heat exchanger model and the methodology introduced in this work represent useful tools for exploring different CSP layouts employing high-temperature heat transfer fluid and indirect TES. In this way, it can pave the way for future research studies and lay the groundwork to explore potential improvements of the new generation of CSP systems. The obtained LCOE values lower than 70 USD/MWh highlight that advanced CSP systems employing sodium and chloride salt TES can represent an economically viable solution and can drive towards the future goal of 5 USD/MWh.

CRediT authorship contribution statement

Salvatore Guccione: Conceptualisation, Methodology, Software, Formal analysis, Data curation, Writing – original draft, Visualisation. **Armando Fontalvo:** Software. **Rafael Guedez:** Resources, Supervision, Funding acquisition. **John Pye:** Conceptualisation, Resources, Supervision, Funding acquisition. **Laura Savoldi:** Conceptualisation, Methodology, Supervision. **Roberto Zanino:** Supervision.

Declaration of competing interest

The authors declare that they have no known competing financial interests or personal relationships that could have appeared to influence the work reported in this paper.

Acknowledgements

This research has been funded by the Australian Solar Thermal Research Institute (ASTRI) with the support of the Erasmus+ programme of the European Union (EU). This work has also received funding from the European Union's Horizon 2020 research and innovation programme under grant agreement No. 952953. We would like to thank the colleagues from The Australian National University for their support and their contribution, particularly, Joe Coventry, Philipe Gunawan Gan, Zebedee Kee, and Shuang Wang.

Appendix A. Auxiliary heat exchanger calculations

See Table A.1 for the auxiliary heat exchanger geometry calculations. Table A.3 shows the tube-side pressure losses coefficients, while shell-side pressure losses coefficients and heat transfer coefficients are shown in Tables A.4 and A.5 respectively.

Table A.2 shows the Turton cost function coefficients.

Table A.1
Auxiliary heat exchanger geometry calculations.

Parameter	Function	Reference
Tube pitch	$P_t = 1.25 \cdot d_o$	Fanaritis and Bevevino (1976)
Bundle-to-shell clearance	$L_{bb} = \frac{12.0+5\cdot(D_{bu}+d_o)}{1000}$	Fanaritis and Bevevino (1976)
Baffle length	$(l_b + t_{baffle}) \cdot (N_b + 1) = L - t_{baffle} + 2 \cdot L_b$	Bott et al. (1994)
Shell-to-baffle diametral clearance	$L_{sb} = \frac{3.1+0.004\cdot D_s}{1000}$	Bott et al. (1994)
Tube-to-baffle diametral clearance	$L_{tb} = 0.0008$	Bott et al. (1994)
Centriangle of baffle cut	$\theta_{ds} = 2\cos^{-1}(1 - 2 \cdot B_c)$	Fanaritis and Bevevino (1976)
Upper centriangle of baffle cut	$\theta_{ctl} = 2\cos^{-1}\left(\frac{D_s-2\cdot L_c}{D_b}\right)$	Bott et al. (1994)
Gross window flow area	$S_{wg} = \frac{\pi}{4}\frac{D_s^2}{N_{sp}}\left(\frac{\theta_{ds}}{2\pi} - \frac{\sin(\theta_{ds})}{2\pi}\right)$	Fanaritis and Bevevino (1976)
Fraction of number of tubes in the baffle window	$F_w = \frac{\theta_{ctl}}{2\pi} - \frac{\sin\theta_{ctl}}{2\pi}$	Bott et al. (1994)
Fraction of tubes in pure crossflow	$F_c = 1 - 2 \cdot F_w$	Bott et al. (1994)
Number of tubes in the window	$N_{tw} = N_t \cdot F_w$	Fanaritis and Bevevino (1976)
Segmental baffle window area occupied by the tubes	$S_{wt} = \frac{N_{tw}}{N_{sp}}\frac{\pi}{4}d_o^2$	Fanaritis and Bevevino (1976)
Net crossflow area through one baffle window	$S_w = S_{wg} - S_{wt}$	Fanaritis and Bevevino (1976)
The number of effective tube rows in crossflow (square layout)	$N_c = D_s\frac{1-2L_c/D_s}{P_t}$	Bott et al. (1994)
The number of effective tube rows in crossflow (triangular layout)	$N_c = D_s\frac{1-2L_c/D_s}{0.866\cdot P_t}$	Bott et al. (1994)
Number of sealing strips per side	$N_{ss} = SS \cdot N_c$	Bott et al. (1994)
Number of effective tube rows in baffle window (square layout)	$N_{cw} = \frac{0.8}{P_t}\left(L_c - \frac{D_s-D_{bu}}{2}\right)$	Bott et al. (1994)
Number of effective tube rows in baffle window (triangular layout)	$N_{cw} = \frac{0.8}{0.866\cdot P_t}\left(L_c - \frac{D_s-D_{bu}}{2}\right)$	Bott et al. (1994)
Shell-side crossflow area	$S_m = \frac{l_b}{N_{sp}}\left(L_{bb} + \frac{D_{bu}}{P_t}(P_t - d_o)\right) = \frac{l_b}{N_{sp}} \cdot L_{cf}$	Fanaritis and Bevevino (1976)
Bypass area between the shell and the tube bundle	$S_b = L_{bb}\frac{l_b}{N_{sp}}$	Fanaritis and Bevevino (1976)
Bypass correction factor	$F_{bp} = \frac{S_b}{S_m}$	Fanaritis and Bevevino (1976)
Shell-to-baffle leakage area	$S_{sb} = \frac{\pi D_s}{N_{sp}}\frac{L_{sb}}{2}\left(\frac{2\pi-\theta_{ds}}{2\pi}\right)$	Fanaritis and Bevevino (1976)
Tube-to-baffle-hole leakage area	$S_{tb} = \frac{N_t}{N_{sp}}\frac{\pi}{4}$	Fanaritis and Bevevino (1976)

Table A.2
Turton cost function and coefficients.

Parameter	Function	Reference
Investment cost	$C_{inv} = C^0_{p,2019} \cdot (B_1 + B_2 \cdot F_M \cdot F_P)$	Turton et al. (2012)
B_1, B_2	1.63, 1.66	Turton et al. (2012)
F_M	3	Turton et al. (2012)
F_P	1	Turton et al. (2012)
Purchased cost (2019)	$C^0_{p,2019} = C^0_p \cdot \frac{CI_{2019}}{CI_{2001}}$	Turton et al. (2012)
CEPCI, CI 2001	397	Turton et al. (2012)
CEPCI, CI 2019	607	Scott (2020)
Purchased cost (2001)	$\log_{10} C^0_p = K_1 + K_2 \cdot \log_{10} A_{HX} + K_3 \cdot [\log_{10} A_{HX}]^2$	Turton et al. (2012)
K_1, K_2, K_3	4.3247, −0.3030, 0.1634	Turton et al. (2012)

Table A.3
Tube-side pressure losses coefficients.

Parameter	Function	Reference
Dimensionless friction factor	$j_f = 8.1274 \cdot Re^{-1.011}$ $(Re \leq 855)$	Fanaritis and Bevevino (1976)
	$j_f = 0.046 \cdot Re^{-0.244}$ $(Re > 855)$	Fanaritis and Bevevino (1976)
Exponent–Pressure losses correlation	$m = 0.25$ $(Re \leq 2100)$	Fanaritis and Bevevino (1976)
	$m = 0.14$ $(Re > 2100)$	Fanaritis and Bevevino (1976)

Table A.4
Shell-side pressure losses coefficients.

Parameter	Function	Reference
Correction factor for bundle bypass	$R_B = \exp(-3.7 \cdot F_{bp} \cdot (1 - r_{ss}^{1/3}))$	Bott et al. (1994)
Correction factor for baffle leakage	$R_L = \exp(-1.33 \cdot (1 + r_s)) \cdot (r_{lm})^x$	Bott et al. (1994)
Pressure drop due to crossflow	$\Delta p_c = (N_b - 1) \cdot \Delta p_{b,i} \cdot R_B \cdot R_L$	Bott et al. (1994)
Pressure drop due to window region	$\Delta p_w = \frac{2+0.6 \cdot N_{cw}}{2 \cdot S_m \cdot S_w \cdot \rho_{cold}} \cdot \dot{m}^2_{cold}$	Bott et al. (1994)
Pressure drop due to entrance and exit regions	$\Delta p_e = 2 \cdot \Delta p_{b,i} \cdot R_B \cdot \left(1 + \frac{N_{cw}}{N_c}\right)$	Bott et al. (1994)
Ideal tube bank pressure drop	$\Delta p_{b,i} = N_c \cdot K_f \cdot \frac{\rho_{cold} \cdot v^2_{shell}}{2}$ where:	Bott et al. (1994)
Friction factor (square layout)	$K_f = 0.272 + \frac{0.207 \cdot 10^3}{Re} + \frac{0.102 \cdot 10^3}{Re^2} - \frac{0.286 \cdot 10^3}{Re^3}$ $(Re \leq 2300)$	Bott et al. (1994)
	$K_f = 0.267 + \frac{0.249 \cdot 10^4}{Re} - \frac{0.927 \cdot 10^7}{Re^2} + \frac{10^{10}}{Re^3}$ $(2300 < Re \leq 2 \cdot 10^6)$	Bott et al. (1994)
Friction factor (triangular layout)	$K_f = 11.474 \cdot Re^{-0.34417}$ $(Re \leq 4000)$	Bott et al. (1994)
	$K_f = 0.245 + \frac{0.339 \cdot 10^4}{Re} - \frac{0.984 \cdot 10^7}{Re^2} + \frac{0.133 \cdot 10^{11}}{Re^3} - \frac{0.599 \cdot 10^{13}}{Re^4}$ $(4000 < Re \leq 2 \cdot 10^6)$	Bott et al. (1994)

Table A.5
Shell-side heat transfer coefficients.

Parameter	Function	Reference
Ideal heat transfer coefficient	$h_{s,id} = \frac{Nu_{cold} \cdot \lambda_{cold}}{d_o}$ where:	
Nusselt number shell-side	$Nu_{cold} = a \cdot Re^m_{cold} \cdot Pr^{0.34}_{cold} \cdot \left(\frac{\mu_{cold,bulk}}{\mu_{cold,wall}}\right)^{0.26}$	Bott et al. (1994)
Nusselt correlation constants (square layout)	$a = 0.742,\ m = 0.431$ $(Re \leq 300)$	Bott et al. (1994)
	$a = 0.211,\ m = 0.651$ $(300 < Re \leq 2 \cdot 10^5)$	Bott et al. (1994)
	$a = 0.116,\ m = 0.7$ $(2 \cdot 10^5 < Re \leq 2 \cdot 10^6)$	Bott et al. (1994)
Nusselt correlation constants (triangular layout)	$a = 1.309,\ m = 0.36$ $(Re \leq 300)$	Bott et al. (1994)
	$a = 0.273,\ m = 0.635$ $(300 < Re \leq 2 \cdot 10^5)$	Bott et al. (1994)
	$a = 0.124,\ m = 0.7$ $(2 \cdot 10^5 < Re \leq 2 \cdot 10^6)$	Bott et al. (1994)
Segmental baffle window correction factor	$J_C = 0.55 + 0.72 \cdot F_c$	Bott et al. (1994)
Baffle leakage correction factor	$J_L = 0.44 \cdot (1 - r_s) + (1 - 0.44 \cdot (1 - r_s)) \cdot \exp(-2.2 \cdot r_{lm})$ where:	Bott et al. (1994)
	$r_{lm} = \frac{S_{sb} + S_{tb}}{S_m}$	Bott et al. (1994)
	$r_s = \frac{S_{sb}}{S_{sb} + S_{tb}}$	Bott et al. (1994)
	$x = 0.8 - 0.15 \cdot (1 + r_s)$	Bott et al. (1994)
Bundle bypass correction factor	$J_B = \exp(-1.35 \cdot F_{bp} \cdot (1 - (2 \cdot r_{ss})^{1/3}))$ where:	Bott et al. (1994)
	$r_{ss} = N_{ss}/N_c$	Bott et al. (1994)

Appendix B. Auxiliary system model calculations

B.1. Receiver auxiliary calculations

Fig. B.1 shows the curves of net flux and flux limit of the receiver at different design cases.

B.2. Cost calculations

Cost functions implemented in this work for the CAPEX and OPEX calculations of the CSP plant are described in Table B.1.

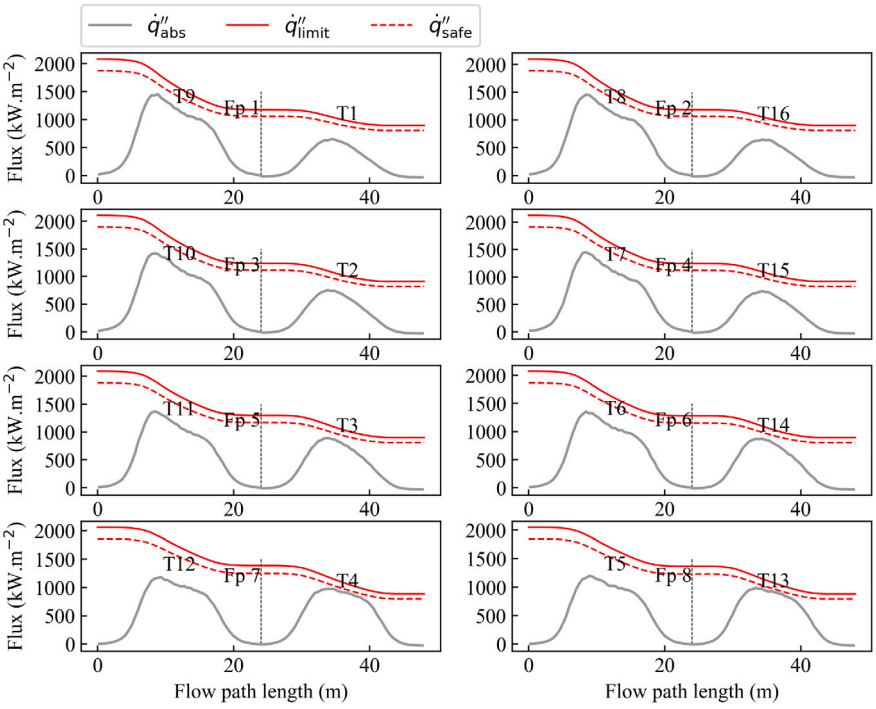

Fig. B.1. Curves of net flux and flux limit at different cases.

Table B.1
Cost functions of the CSP plant subsystems.

Parameter	Function
Capital expenditure	$CAPEX = C_{dir} + C_{indir}$
Direct costs	$C_{dir} = (C_{field} + C_{site} + C_{tower} + C_{rec} + C_{HX} + C_{TES} + C_{BOP} + C_{block}) \cdot (1 + f_{contingency})$
Indirect costs	$C_{indir} = C_{dir} \cdot f_{EPC} + C_{land}$
Heliostat field	$C_{field} = c_{field} \cdot A_{field}$
Site improvement	$C_{site} = c_{site} \cdot A_{field}$
Tower	$C_{tower} = C_{tower,ref} \cdot e^{(c_{tower} \cdot H_{tower})}$
Receiver	$C_{receiver} = C_{receiver,ref} \cdot (A_{receiver}/A_{receiver,ref})^{e_{receiver}}$
Sodium–salt HX	$C_{HX} = c_{H230} \cdot F_{ma} \cdot M_a \cdot A_{HX}$
Thermal energy storage	$C_{TES} = c_{TES} \cdot E_{max,TES}$
Balance of plant	$C_{BOP} = c_{BOP} \cdot P_{gross}$
Power block	$C_{block} = c_{block} \cdot P_{gross}$
Land	$C_{land} = c_{land} \cdot A_{land}$
Operating expenditure	$OPEX = c_{OM,fix} \cdot P_{net} + c_{OM,prod} \cdot EPY$

Table B.2
Power block off-design coefficients.[a]

Parameter	Function
Cooling power	$v_w = 0.0226 \cdot (T_{amb} - 273.15)\ (0.98 \le load \le 1)$ $v_w = -0.0009 \cdot (T_{in} - 273.15) + 0.9158 \cdot load + 0.0166 \cdot (T_{amb} - 273.15)\ (load < 0.98)$ $v_w = -0.2137 \cdot load + 0.0299 \cdot (T_{amb} - 273.15)\ (load > 1)$
Gross power	$k_w = 1.00477 \cdot (T_{in}/T_{in,des})\ (load > 1, T_{amb} < 294.15)$ $k_w = 0.628065 \cdot (T_{in}/T_{in,des}) - 0.0520314 \cdot T_{amb} + (3.70578e-4) \cdot T_{amb}^2 - (6.42937e-7) \cdot T_{amb}^3\ (load > 1, T_{amb} \ge 294.15)$ $k_w = 0.421643 \cdot (T_{in}/T_{in,des}) + 0.934566 \cdot load - 0.00124385 \cdot T_{amb}\ (load \le 1)$
Thermal power	$k_q = 1.92783 - 0.945337 \cdot (T_{in}/T_{in,des})\ (load > 1, T_{amb} < 294.15)$ $k_q = -0.0295685 \cdot T_{amb} + (2.36193e-4) \cdot T_{amb}^2 - (4.2183e-7) \cdot T_{amb}^3\ (load > 1, T_{amb} \ge 294.15)$ $k_q = (4.42606e-4) \cdot T_{amb} + 0.844403 \cdot load\ (load \le 1)$

[a]Interpolated from sCO_2 Cycle Integration Macro, SAM v14.02.2020.

B.3. Power block auxiliary calculations

Table B.2 summarises the equations of the coefficients adopted to estimate the off-design performance of the power block.

References

Armijo, K., 2019. Design basis for a 2.0 MWth liquid-HTF pilot- scale CSP system. In: Presentation - Asia-Pacific Solar Research Conference. Canberra, Australia.

Asselineau, C.-A., Logie, W., Pye, J., Venn, F., Wang, S., Coventry, J., 2020. Design of a heliostat field and liquid sodium cylindrical receiver for the Gen3 liquids pathway. In: SolarPACES. Albuquerque.

Barua, B., McMurtrey, M., Rupp, R.E., Messner, M.C., 2020. Design Guidance for High Temperature Concentrating Solar Power Components. Tech. Rep., Argonne National Lab. (ANL), Argonne, IL (United States).

Bell, K.J., 1988. Delaware method for shellside design. In: Shah, R.K., Subbarao, E.C., Mashelkar, R.A. (Eds.), Heat Transfer Equipment Design. Hemisphere, Washington,

DC, pp. 145–166.
Benoit, H., Spreafico, L., Gauthier, D., Flamant, G., 2016. Review of heat transfer fluids in tube-receivers used in concentrating solar thermal systems: Properties and heat transfer coefficients. Renew. Sustain. Energy Rev. 55, 298–315. http://dx.doi.org/10.1016/j.rser.2015.10.059.
Blanco, M.J., Santigosa, L.R., 2017. Advances in Concentrating Solar Thermal Research and Technology. In: Woodhead Publishing Series in Energy.
Bonilla, J., de la Calle, A., Rodríguez-García, M.M., Roca, L., Valenzuela, L., 2017. Study on shell-and-tube heat exchanger models with different degree of complexity for process simulation and control design. Appl. Therm. Eng. 124, 1425–1440. http://dx.doi.org/10.1016/j.applthermaleng.2017.06.129.
Bott, T.R., Hewitt, G.F., Shires, G.L., 1994. Process Heat Transfer. CRC-Press.
Bucher, W., 1983. Investigations and Findings Concerning the Sodium Tank Leakages. Tech. Rep. SSPS TR-5/83, DVFLR (now DLR), SSPS (Small Solar Power Systems) project.
Coventry, J., Andraka, C., Pye, J., Blanco, M., Fisher, J., 2015. A review of sodium receiver technologies for central receiver solar power plants. Sol. Energy 122, 749–762. http://dx.doi.org/10.1016/j.solener.2015.09.023.
de la Calle, A., Bayon, A., Pye, J., 2020. Techno-economic assessment of a high-efficiency, low-cost solar-thermal power system with sodium receiver, phase-change material storage, and supercritical CO2 recompression Brayton cycle. Sol. Energy 199, 885–900. http://dx.doi.org/10.1016/j.solener.2020.01.004.
DOE, 2012. SunShot Vision Study. Tech. Rep. DOE/GO-102012-3037, US Department of Energy (DOE), Office of Energy Efficiency & Renewable Energy, p. 320. http://dx.doi.org/10.2172/1039075.
DOE, 2018. Generation 3 Concentrating Solar Power Systems (Gen3 CSP). United States Department of Energy, URL https://is.gd/5hcxuh (Accessed 10 October 2021).
DOE, 2019. Gen 3 CSP Topic 1–Phase 3 Test Facility Down-Selection Criteria. United States Department of Energy, Office of Energy Efficiency and Renewable Energy, Washington, DC, USA, Internal document provided to project participants.
Drake, C.E., Carp, J.R., 1960. Shell and tube heat exchangers. Chem. Eng. 165–170.
Fanaritis, J.P., Bevevino, J.W., 1976. Designing shell-and-tube heat exchangers. Chem. Eng. 83 (14), 62–71.
Ferruza, D., 2018. Design of Steam Generator Systems for Concentrating Solar Power Plants (Doctoral thesis). Technical University of Denmark.
Ferruzza, D., Kærn, M.R., Haglind, F., 2019. Design of header and coil steam generators for concentrating solar power applications accounting for low-cycle fatigue requirements. Appl. Energy 236 (July 2018), 793–803. http://dx.doi.org/10.1016/j.apenergy.2018.12.030.
Fous, O.J., 1972. Sodium-NaK Engineering Handbook. Volumn I. Sodium Chemistry and Physical Properties. Tech. Rep., US Atomic Energy Commission (AEC), p. 339, URL https://www.osti.gov/biblio/4631555.
Fritsch, A., Frantz, C., Uhlig, R., 2019. Techno-economic analysis of solar thermal power plants using liquid sodium as heat transfer fluid. Sol. Energy 177, 155–162. http://dx.doi.org/10.1016/j.solener.2018.10.005.
González-Gómez, P.A., Gómez-Hernández, J., Briongos, J.V., Santana, D., 2018. Assessment of evaporators using solar salt as heat transfer fluid. AIP Conf. Proc. 2033 (November), http://dx.doi.org/10.1063/1.5067051.
González-portillo, L.F., Albrecht, K., Ho, C.K., 2021. Techno-economic optimization of CSP plants with free-falling particle receivers.
Gunawan Gan, P., Wang, Y., Pye, J., 2021. System Modelling and Optimisation of a Particle-Based CSP System. Tech. Rep. Feb 2021, Australian National University, http://dx.doi.org/10.13140/RG.2.2.15488.15365.
Ho, C.K., 2016. A review of high-temperature particle receivers for concentrating solar power. Appl. Therm. Eng. 109, 958–969. http://dx.doi.org/10.1016/j.applthermaleng.2016.04.103.
Ho, C.K., Iverson, B.D., 2014. Review of high-temperature central receiver designs for concentrating solar power. Renew. Sustain. Energy Rev. 29, 835–846. http://dx.doi.org/10.1016/j.rser.2013.08.099.
Incropera, F.P., Dewitt, D.P., 1981. Fundamentals of Heat Transfer, fourth ed. Wiley, New York.
Jordan, S., Cherdron, W., Malet, J.-C., Rzekiecki, R., Himeno, Y., 1988. Sodium aerosol behavior in liquid-metal fast breeder reactor containments. Nucl. Technol. 81, 183–192. http://dx.doi.org/10.13182/NT88-A34091.
Kee, Z., Pye, J., Coventry, J., 2020. System level analysis of a sodium boiler receiver and PCM storage CSP plant using SolarTherm. AIP Conf. Proc. 2303 (1), 190021. http://dx.doi.org/10.1063/5.0029494, Proceedings of SolarPACES 2019.
Logie, W.R., Pye, J.D., Coventry, J., 2018. Thermoelastic stress in concentrating solar receiver tubes: A retrospect on stress analysis methodology, and comparison of salt and sodium. Sol. Energy 160, 368–379.
MCCE, 1987. Lessons from the SSPS-CRS Sodium Fire Incident. Tech. Rep. SSPS TR-3/87, Motor Columbus Consulting Engineers Inc., Baden, Switzerland, International Energy Agency: Small Solar Power Systems (SSPS) project.
Mehos, M., Turchi, C., Jorgenson, J., Denholm, P., Ho, C.K., Armijo, K., 2016. On the Path to SunShot: Advancing Concentrating Solar Power Technology, Performance, and Dispatchability. SunShot, U. S. Department of Energy, pp. 1–66.
Mohan, G., Venkataraman, M., Gomez-Vidal, J., Coventry, J., 2018. Assessment of a novel ternary eutectic chloride salt for next generation high-temperature sensible heat storage. Energy Convers. Manage. 167, 156–164. http://dx.doi.org/10.1016/j.enconman.2018.04.100.
Murphy, C., Sun, Y., Cole, W., Maclaurin, G., Turchi, C., Mehos, M., 2019. The Potential Role of Concentrating Solar Power within the Context of DOE's 2030 Solar Cost Targets. NREL Technical Report - NREL/TP-6A20-71912 (NREL/TP-6A20-71912), p. 137, URL https://www.nrel.gov/docs/fy19osti/71912.pdf.
Niedermeier, K., Marocco, L., Flesch, J., Mohan, G., Coventry, J., Wetzel, T., 2018. Performance of molten sodium vs. molten salts in a packed bed thermal energy storage. Appl. Therm. Eng. 141, 368–377. http://dx.doi.org/10.1016/j.applthermaleng.2018.05.080.
Price, H., Mehos, M., Kearney, D., Cable, R., Kelly, B., Kolb, G., Morse, F., 2021. Concentrating solar power best practices. In: Concentrating Solar Power Technology. pp. 725–757. http://dx.doi.org/10.1016/b978-0-12-819970-1.00020-7.
Scott, J., 2020. Chemical engineering plant cost index: 2019 annual value. URL https://www.chemengonline.com/2019-chemical-engineering-plant-cost-index-annual-average/.
Scott, P., Alonso, A.D.L.C., Hinkley, J.T., Pye, J., 2017. SolarTherm: A Flexible modelica-based simulator for CSP systems. AIP Conf. Proc. 1850 (June 2017), http://dx.doi.org/10.1063/1.4984560.
Shweta, Y.K., Jagadish, S.B., Manjunath, M.B., 2014. Analysis comparing performance of a conventional shell and tube heat exchanger using Kern, Bell and Bell Delaware method. Int. J. Res. Eng. Technol. 486–496. http://dx.doi.org/10.15623/ijret.2014.0315093.
Simons, E.M., Basham, S.J., 1966. Control of coolant purity in sodium-cooled reactors. In: Annual Winter Meeting of ASME. New York, Document 66-WA/NE 17.
Sinnott, R.K., 1999. Coulson & Richardson's Chemical Engineering: Chemical Engineering Design: Volume 6, third ed. Butterworth-Heinemann.
Thulukkanam, K., 2013. Heat Exchanger Design Handbook, second ed. CRC Press, pp. 237–336.
Trevisan, S., Guédez, R., Laumert, B., 2020. Thermo-economic optimization of an air driven supercritical CO2 Brayton power cycle for concentrating solar power plant with packed bed thermal energy storage. Sol. Energy 211 (October), 1373–1391. http://dx.doi.org/10.1016/j.solener.2020.10.069.
Turchi, C.S., Boyd, M., Kesseli, D., Kurup, P., Mehos, M., Neises, T., Sharan, P., Wagner, M.J., Wendelin, T., 2019. CSP systems analysis - final project. Nrel/TP-5500-72856 (May). URL www.nrel.gov/publications.
Turton, R., Bailie, R.C., Whiting, W.B., Shaeiwitz, J.A., Bhattacharyya, D., 2012. Cost equations and curves for the CAPCOST program. In: Analysis, Synthesis and Design of Chemical Processes, third ed. Prentice-Hall, pp. 923–954.
Vast Solar, 2015. Chemical leak successfully managed at solar research & development facility outside Forbes NSW. Media release. URL https://is.gd/WY7dAu. (Accessed via web.archive.org, 10 October 2021).
Wang, S., Asselineau, C.-A., Logie, W.R., Pye, J., Coventry, J., 2021. MDBA: An accurate and efficient method for aiming heliostats. Sol. Energy 225, 694–707.
Wolf, F.G., 2001. Operationalizing and testing normal accident theory in petrochemical plants and refineries. Prod. Oper. Manage. 10 (3), 292–305. http://dx.doi.org/10.1111/j.1937-5956.2001.tb00376.x.
Wood, C., Drewes, K., 2019. Vast Solar: Improving performance and reducing cost and risk using high temperature modular arrays and sodium heat transfer fluid. In: Proceedings of the SolarPaces 2019 Conference, 4 pp.
Zheng, M., Zapata, J., Asselineau, C.-A., Coventry, J., Pye, J., 2020. Analysis of tubular receivers for concentrating solar tower systems with a range of working fluids, in exergy-optimised flow-path configurations. Sol. Energy 211, 999–1016. http://dx.doi.org/10.1016/j.solener.2020.09.037.
Zurita, A., Mata-Torres, C., Valenzuela, C., Felbol, C., Cardemil, J.M., Guzmán, A.M., Escobar, R.A., 2018. Techno-economic evaluation of a hybrid CSP+PV plant integrated with thermal energy storage and a large-scale battery energy storage system for base generation. Sol. Energy 173 (July), 1262–1277. http://dx.doi.org/10.1016/j.solener.2018.08.061.